

## Research Paper

# VMD and CNN-Based Classification Model for Infrasound Signal

Quanbo LU, Mei LI\*

*School of Information Engineering, China University of Geosciences  
Beijing, China*

\*Corresponding Author e-mail: maggieli@cugb.edu.cn

(received November 4e, 2022; accepted April 1, 2023)

Infrasound signal classification is vital in geological hazard monitoring systems. The traditional classification approach extracts the features and classifies the infrasound events. However, due to the manual feature extraction, its classification performance is not satisfactory. To deal with this problem, this paper presents a classification model based on variational mode decomposition (VMD) and convolutional neural network (CNN). Firstly, the infrasound signal is processed by VMD to eliminate the noise. Then fast Fourier transform (FFT) is applied to convert the reconstructed signal into a frequency domain image. Finally, a CNN model is established to automatically extract the features and classify the infrasound signals. The experimental results show that the classification accuracy of the proposed classification model is higher than the other model by nearly 5%. Therefore, the proposed approach has excellent robustness under noisy environments and huge potential in geophysical monitoring.

**Keywords:** infrasound signal; variational mode decomposition; convolutional neural network; fast Fourier transform.



Copyright © 2023 The Author(s).  
This work is licensed under the Creative Commons Attribution 4.0 International CC BY 4.0  
(<https://creativecommons.org/licenses/by/4.0/>).

## 1. Introduction

Infrasound ( $\leq 20$  Hz) is generated by natural disasters and human activities, including earthquakes, tsunamis, mudslides, tornados, volcano eruptions, nuclear explosions, missile launching, and ship navigation. Infrasound propagates through the atmosphere thousands of kilometers. The attenuation in the propagation process is small and its loss is less than a few thousandths (GI, BROWN, 2017; DE ANGELIS *et al.*, 2019). Consequently, infrasound can serve as monitoring properties for geological hazards.

Infrasound has been widely applied in recent years in geological hazard monitoring. Many scholars began to pay attention to this topic. LENG *et al.* (2017) presented a debris-flow monitoring approach, which relied on the characteristics of infrasound signal. ZHANG *et al.* (2020) designed an infrasound-based device for monitoring landslides. PERTTU *et al.* (2020) demonstrated the use of remote infrasound in estimating the height of volcanic plumes. WITSIL and JOHNSON (2020) extracted the infrasound features from the time and frequency domains. Then the infrasound features were clustered using the k-means algorithm. HAM *et al.*

(2008) used radial basis function (RBF) network as the subnetworks of a parallel neural network classifier bank to classify different infrasound events. With the wide application of data mining classification algorithm in the signal, feature extraction can be performed on the signal to achieve a better classification effect. ZHU *et al.* (2017) employed Hilbert-Huang transform (HHT) to extract the infrasound related to earthquakes. LIU *et al.* (2014) respectively used three kinds of feature extraction techniques (spectral entropy, discrete wavelet transformation (DWT) and HHT) to extract the feature vector of four kinds of infrasound signals. The signal feature extracted by back propagation neural network and support vector machines (SVM) for classification, all of which have higher classification accuracy, were studied (THÜRING *et al.*, 2015; IEZZI *et al.*, 2019).

LIU *et al.* (2021) constructed the feature vector set and applied the K-nearest neighbor (KNN) to identify the landslide infrasound signal. LI *et al.* (2016) performed spectral entropy on the infrasound signals to extract the features and classify the infrasound events. WITSIL *et al.* (2022) introduced a physics-based method that propagates infrasound sources through re-

alistic atmospheres. HUPE *et al.* (2022) provided infrasound data products that can serve as observational data for the atmospheric studies and scientific and civilian applications. WATSON *et al.* (2022) reviewed the progress and future direction of volcano infrasound research. GARCIA *et al.* (2022) presented the first detection of seismic infrasound from a large-magnitude earthquake on a balloon network of barometers. ECKEL *et al.* (2023) used pattern recognition techniques on infrasound signals to monitor volcanic activity. YANG *et al.* (2022) reviewed the research progress on infrasound generation mechanism, monitoring technology, and application. COFFERB and PARKER (2022) studied the infrasound signals in simulated nontornadic and pre-tornadic phase of the tornadic supercells. AS-MING *et al.* (2022) overviewed methods and algorithms for detecting, locating, and discriminating seismic and infrasound events. ZHANG *et al.* (2022) provided an infrasound source localization algorithm for improving the location accuracy of the gas pipeline leakage detection system. GARCIA *et al.* (2021) used coupled pressure/ground deformation methods to search for the infrasound signal. However, it can be difficult to automatically extract the features and classify the infrasound signals with all the above presented approaches.

To address it, a novel method based on variational mode decomposition (VMD) and convolutional neural network (CNN) is proposed for infrasound signal classification. Firstly, the infrasound signal is processed by VMD to eliminate the noise, and fast Fourier transform (FFT) is employed to convert the reconstructed signal into a frequency domain image. Then the obtained frequency domain image is used as the input of the CNN. Finally, a CNN model is established to automatically extract the features and classify the infrasound signals.

The rest of this paper is organized as follows. In Sec. 2, the basic theory of VMD and CNN used in this paper is shortly described. Section 3 compares the performance of the described methods in an experiment. Further, the experiment results are shown through the analysis of different methods in Sec. 4. Finally, conclusions are drawn in Sec. 5.

## 2. Methods

### 2.1. VMD

VMD decomposes an input signal  $f$  into a group of discrete modes  $u_k$ , and each mode is compressed to obtain a central frequency  $w_k$  (DRAGOMIRETSKIY, ZOZZO, 2014). The constrained variational model is shown in Eq. (1):

$$\min_{\{u_k\}, \{w_k\}} \left\{ \sum_k \left\| \partial_t \left[ \left( \delta(t) + \frac{j}{\pi t} \right) u_k(t) \right] e^{-jw_k t} \right\|_2^2 \right\} \quad (1)$$

s.t.  $\sum_k u_k = f,$

where  $\{u_k\} = \{u_1, \dots, u_k\}$  are the  $k$  mode components obtained by decomposition and  $\{w_k\} = \{w_1, \dots, w_k\}$  are the center frequencies of each mode;  $\delta(t)$  is the Dirac delta function.

The augmented Lagrange function is introduced by Eq. (2), and the solution of Eq. (1) is obtained by the alternating direction method of multipliers:

$$L(\{u_k\}, \{w_k\}, \lambda) = \alpha \sum_k \left\| \partial_t \left[ \left( \delta(t) + \frac{j}{\pi t} \right) u_k(t) \right] e^{-jw_k t} \right\|_2^2 + \left\| f(t) - \sum_k u_k(t) \right\|_2^2 + \left\langle \lambda(t), f(t) - \sum_k u_k(t) \right\rangle, \quad (2)$$

where secondary penalty item  $\alpha$  ensures the signal reconstruction accuracy under the Gaussian noise, the Lagrange multiplier  $\lambda$  is the constraint value, and  $\langle \rangle$  is the inner product calculation.

The VMD algorithm process is as follows:

- Step 1. Set the number of decomposition modes. Initialize frequency domain  $\{\widehat{u}_k^1\}$ , center frequency  $\{w_k^1\}$ , and the Lagrange multipliers  $\widehat{\lambda}^1$ . Modal  $u_k$  and center frequency  $w_k$  are calculated by Eq. (3) and Eq. (4). Initialize,  $\widehat{\lambda}^1$ ,  $n \leftarrow 0$ .
- Step 2. Set  $n \leftarrow n + 1$ ,  $k \leftarrow k + 1$  and execute the whole cycle. Update  $\widehat{u}_k$  and  $w_k$  for all  $w \geq 0$  to reach the preset decomposition number. When  $k = K$ , the cycle ends. The updated formula of the narrow-band component and the corresponding center frequency is:

$$\widehat{u}_k^{n+1}(w) = \frac{\widehat{f}(w) - \sum_{i < k} \widehat{u}_i^{n+1}(w) - \sum_{i > k} \widehat{u}_i^n(w) + \frac{\widehat{\lambda}^n(w)}{2}}{1 + 2\alpha(w - w_k^n)^2}, \quad (3)$$

$$w_k^{n+1} = \frac{\int_0^\infty w |\widehat{u}_k^{n+1}(w)|^2 dw}{\int_0^\infty |\widehat{u}_k^{n+1}(w)|^2 dw}. \quad (4)$$

- Step 3. Update  $\lambda$  according to the formula:

$$\widehat{\lambda}^{n+1}(w) \leftarrow \widehat{\lambda}^n(w) + \tau \left( \widehat{f}(w) - \sum_k \widehat{u}_k^{n+1}(w) \right). \quad (5)$$

- Step 4. Return to step 2 and repeat the above process until the whole iterative process meets the constraints, and a series of narrow-band eigenmode component signals are obtained. Equation (6) is the constraint condition, where  $\varepsilon$  is set to 10<sup>-6</sup>:

$$\sum_k \left\| \widehat{u}_k^{n+1} - \widehat{u}_k^n \right\|_2^2 / \left\| \widehat{u}_k^n \right\|_2^2 < \varepsilon. \quad (6)$$

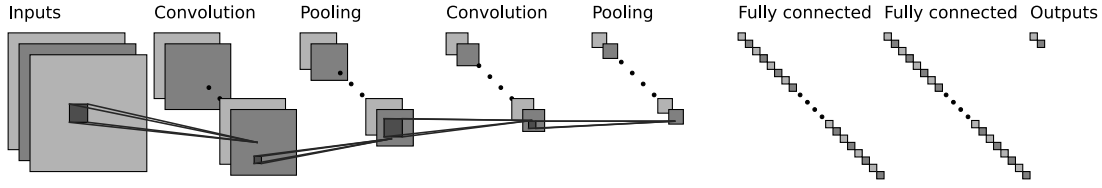


Fig. 1. Structure of CNN.

## 2.2. CNN

CNN is an important part of deep neural networks (LAWRENCE *et al.*, 1997). It is composed of a multi-level structure that can be trained. Due to its strong feature extraction ability, CNN has been widely used in the field of signal processing. Each level of CNN generally consists of a convolution layer, pooling layer, fully connected layer, and softmax layer. The feature extraction is obtained by multiple alternating operations. Finally, through the fully connected layer and classifier, the infrasound signal classification is realized. The structure of CNN is shown in Fig. 1.

### 2.2.1. Convolution layer

The convolution layer uses convolution kernels to perform convolution on input data and obtains the feature maps. Each convolution kernel outputs a feature map, which is conformed to a class of the extracted features. The mathematical expression of the convolution is as follows:

$$x_j^l = f\left(\sum_{i \in M_j} x_i^{l-1} * k_{ij}^l + b_j^l\right), \quad (7)$$

where  $l$  is the  $l$ -th convolution layer,  $x_i^l$  is the  $l$ -th output,  $x_i^{l-1}$  is the  $l$ -th input,  $k_{ij}^l$  is the weight matrix,  $b_j^l$  is the bias term,  $M_j$  is the  $j$ -th convolutional region of the  $l-1$ -th feature map, and  $f(\cdot)$  is the activation function. In the CNN model, the activation function usually uses the ReLU function. The activation function is represented as:

$$f(x) = \max(0, x). \quad (8)$$

### 2.2.2. Pooling layer

When the convolution layer finishes the convolution, the pooling layer performs downsampling on the input eigenvectors through the pooling kernels. It can reduce the dimension of the data and further highlight the extracted features. Generally, the pooling operations are divided into two types: max pooling and average pooling. The pooling is expressed as:

$$x_{i+1} = f(\beta^* \text{down}(x_i) + b), \quad (9)$$

where  $x_i$  is the input,  $\text{down}(\cdot)$  is the pooling function,  $\beta$  is the multiplicative bias,  $b$  is the additive bias, and  $f(\cdot)$  is the activation function.

### 2.2.3. Fully connected layer and softmax layer

The fully connected layer and softmax layer are applied in the classification stage of CNN. It can connect the feature maps obtained after a series of convolution and pooling operations into the one-dimensional feature vector. The classification results are gained by the softmax layer. The mathematic model of the fully connected layer and softmax layer can be described as:

$$y^k = \text{softmax}(w^k * x^{k-1} + b^k), \quad (10)$$

where  $x^{k-1}$  is the input of the fully connected layer,  $y^k$  is the output of the fully connected layer,  $w^k$  is the weight coefficient,  $b^k$  is the additive bias, and  $k$  is the  $k$ -th network layer.

## 2.3. The proposed approach

Infrasound signals collected from the International Monitoring System (IMS) usually exhibit non-linear and non-stationary characteristics. It makes feature extraction difficult and the classification performance unsatisfactory (MAYER *et al.*, 2020). This paper proposes an intelligent infrasound signal classification method based on VMD and CNN. The flowchart of the proposed method is shown in Fig. 2. The general procedures are summarized as follows:

- Step 1. Collect the infrasound signal with sensors.
- Step 2. The collected infrasound signal data is converted into U modes using VMD to eliminate the noise.
- Step 3. FFT is applied to convert the reconstructed signal into a frequency domain image.
- Step 4. The preprocessing data is separated into the training and testing samples. The proposed approach is used to extract deep features from the training samples based on CNN. The trained model is deployed for the infrasound signal classification.
- Step 5. The  $t$ -distributed stochastic neighbor embedding ( $t$ -SNE) is employed to visualize features in softmax layers (VAN DER MAATEN, HINTON, 2008).
- Step 6. The classification results are presented to compare the performance of different methods.

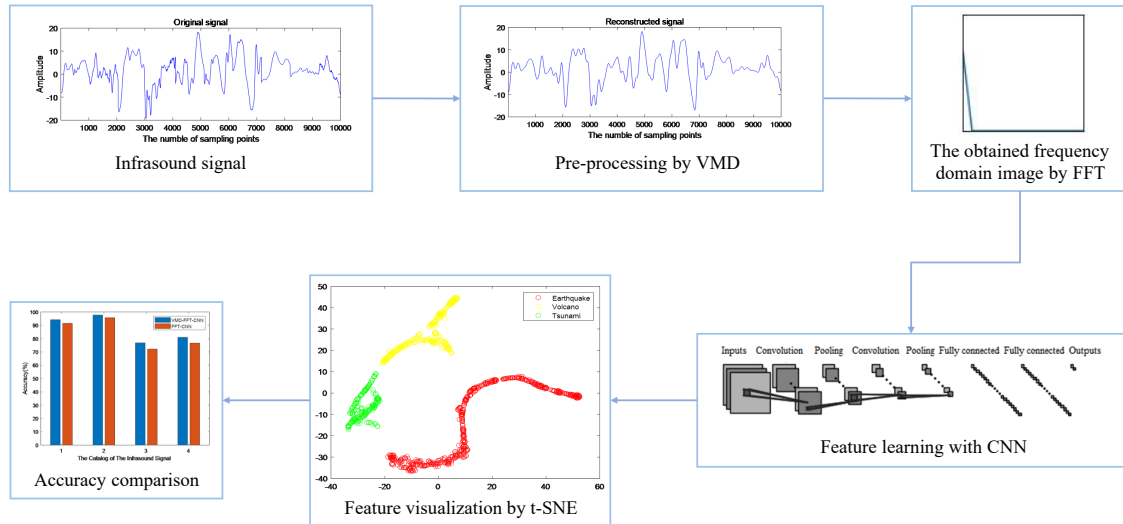


Fig. 2. Flowchart of the proposed approach.

2.4. Data set

The data used in this study comes from IMS with the help of the Comprehensive Nuclear-Test-Ban Treaty Beijing National Data Center. Three categories of infrasound events are classified in this study. The data are collected from six different infrasound sensor arrays with different locations around the world. This study uses 611 sets of data. Table 1 shows the details of infrasound data collected from different areas. The three categories of infrasound events are earthquake, tsunami, and volcano. The sampling frequency of all 611 infrasound signal recordings is 20 Hz. The map of the infrasound stations is showed in Fig. 3.

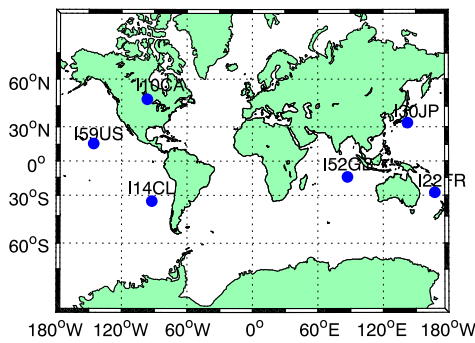


Fig. 3. Map of the infrasound stations.

3. Experiments

3.1. Experiments setup

According to the description of CNN in Subsec. 2.2, the main parameters of the CNN are summarized in Table 2. The simulation verification is devoted to applying the infrasound signal data mentioned above to evaluate the feature learning performance of the proposed CNN model. Every infrasound signal contains 10 400 data points. The data sets are divided into training samples and testing samples. The size of the input

Table 2. The parameters of CNN.

No. of layer	Layer type	Kernel size	Filters
1	Convolution 1	10 × 10	4
2	Maxpooling 1	3 × 3	–
3	Convolution 2	5 × 5	4
4	Maxpooling 2	3 × 3	–
5	Convolution 3	3 × 3	8
6	Convolution 4	3 × 3	8
7	Convolution 5	3 × 3	8
8	Maxpooling 3	3 × 3	–
9	Flattened	–	–
10	Fully-connected	–	–
11	Softmax	–	–

Table 1. Infrasound data summary.

Event type	Data source (IMS Station Code)	Geographic coordinate	Number of signals	Total	Sampling frequency [Hz]
Earthquake	I14CL	(-33.65, -78.79)	74	203	20
	I30JP	(35.31, 140.31)	124		20
	I59US	(19.59, -155.89)	6		20
Tsunami	I10CA	(50.20, -96.03)	4	218	20
	I22FR	(-22.18, 166.85)	53		20
	I30JP	(35.31, 140.31)	113		20
	I52GB	(-7.38, 72.48)	66		20
Volcano	I30JP	(35.31, 140.31)	189	189	20

map to the CNN model is  $129 \times 129 \times 1$ . The iteration number is 50.

### 3.2. Data preprocessing

The VMD is employed to decompose the infrasound signal. When the mode number  $U$  is different, the center frequency is different. The relationship between  $U$  and the center frequency is depicted in Fig. 4.

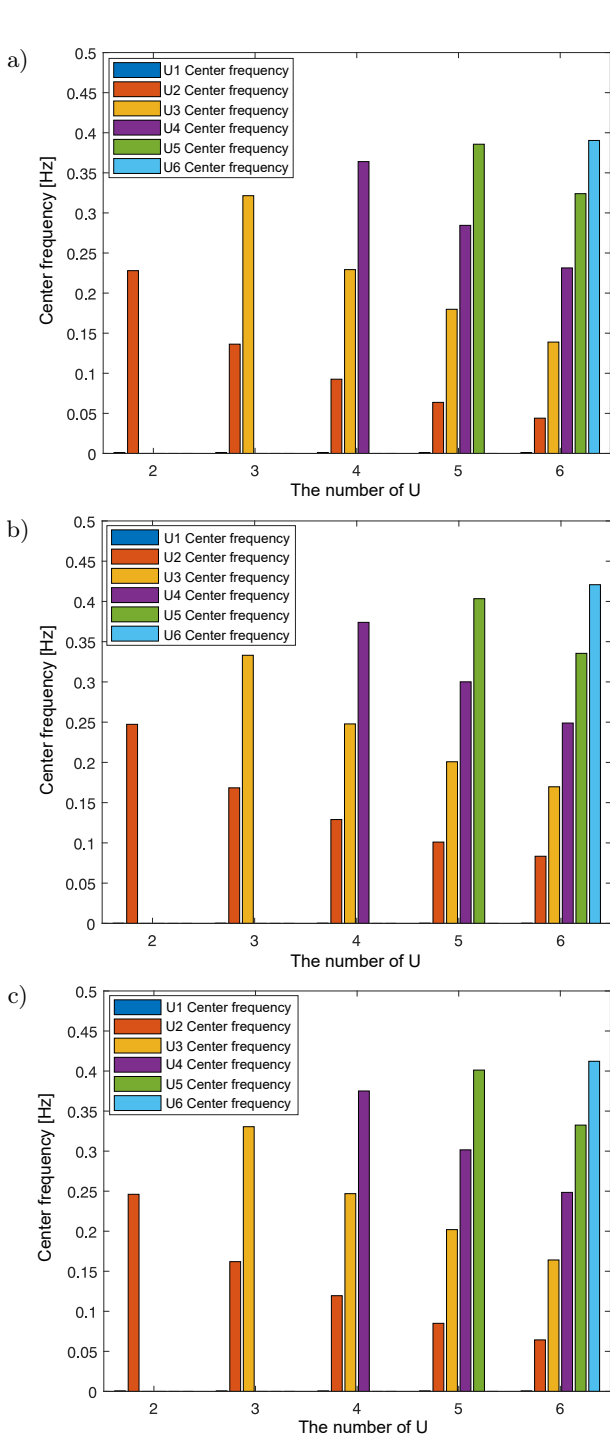


Fig. 4. Relationship between mode number and center frequency: a) earthquake after VMD; b) tsunami after VMD; c) volcano after VMD.

In the earthquake, tsunami, and volcano decomposition results, when the value of  $U$  starts from 6, the center frequency is close. This is an over-decomposition phenomenon. Hence, the  $U$  value taken in the test is 5. Based on VMD experience, the balance parameter constrained by data fidelity adopts the default value of 2000, and the time step of double rise is 0.1. Figure 5 demonstrates the results of the original signal

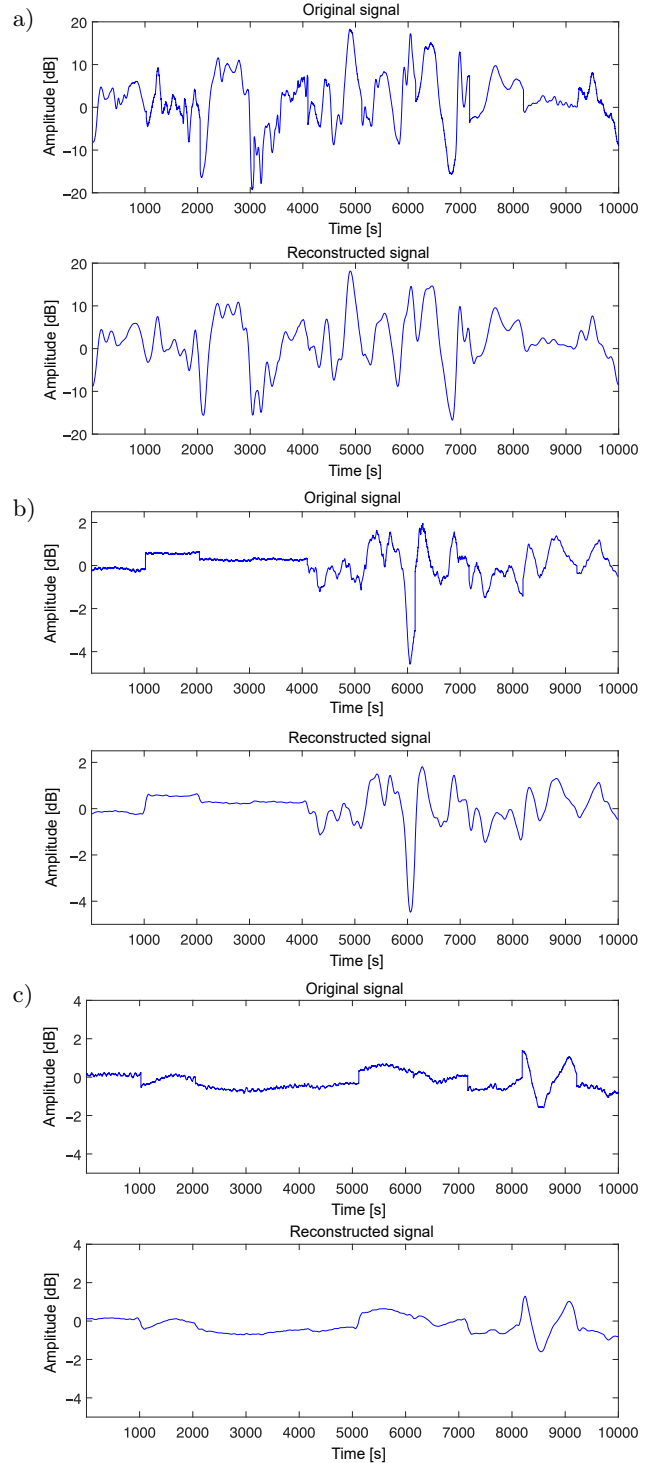


Fig. 5. Original signal and reconstructed signal: a) earthquake; b) tsunami; c) volcano.

and reconstructed signal. Compared with the original signal, the reconstructed signal eliminates the noise. Then, FFT is employed to convert the reconstructed signal into the frequency domain.

### 3.3. Model application results and analysis

In this study, the CNN structure contains five convolutional layers, three pooling layers, a flattened layer, a fully connected layer, and a softmax layer. The parameters on each layer are presented in Table 2, which are determined based on comparative trials and ex-

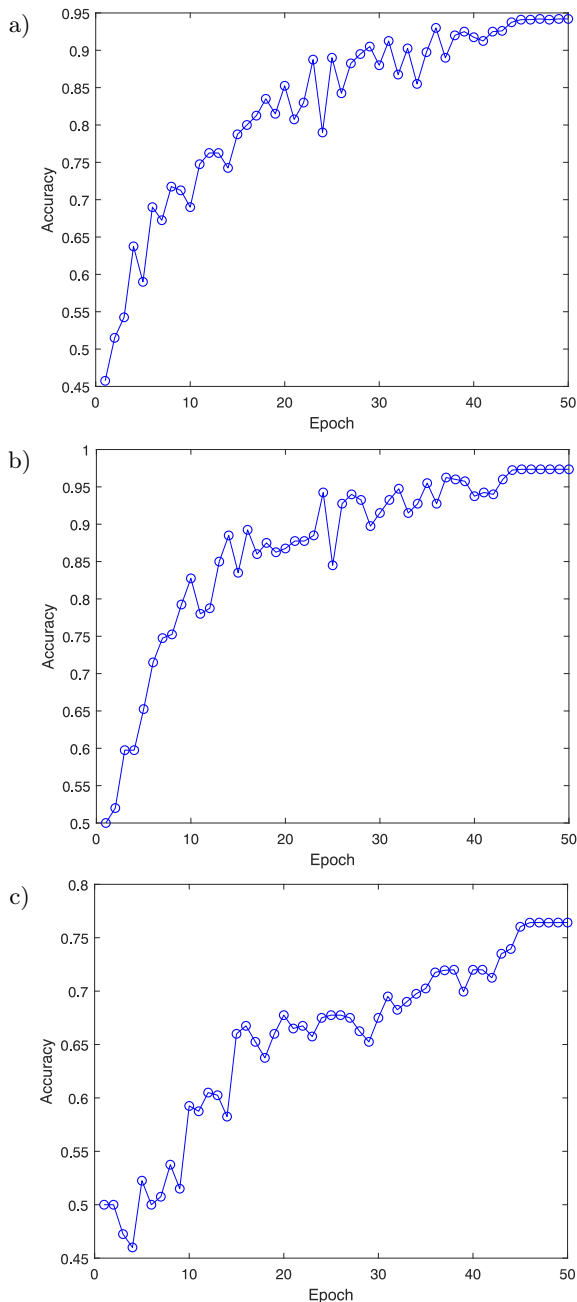


Fig. 6. Classification accuracy of the 2-class catalog after VMD-FFT-CNN: a) earthquake and tsunami; b) earthquake and volcano; c) tsunami and volcano.

perience. The CNN model is written in Python 3.5 and runs on Windows 64 with the Core (TM) i5-8250U CPU and 8G RAM.

The classification accuracy of the 2-class catalog after VMD-FFT-CNN is presented in Fig. 6. Figure 7 shows the classification accuracy of the 3-class catalog after VMD-FFT-CNN, respectively.

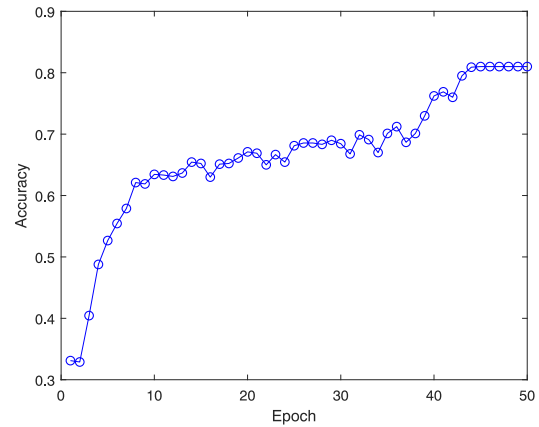


Fig. 7. Classification accuracy of the 3-class catalog after VMD-FFT-CNN.

In order to better illustrate the feature learning process of the proposed model, the t-SNE technique is applied to visualize the output of the softmax layer. It is a machine learning algorithm for high dimensional data visualization using a non-linear dimensionality reduction technique. The feature visualizations of the 2-class catalog and 3-class catalog after VMD-FFT-CNN are shown in Figs. 8 and 9, respectively. It can be seen that the distribution of the points with the same color is relatively closely grouped and easy to distinguish.

To better analyze the classification performance of the proposed method, the infrasound signals are processed by FFT-CNN. The classification accuracy of the 2-class catalog after FFT-CNN is presented in Fig. 10. Figure 11 shows the classification accuracy of the 3-class catalog after FFT-CNN. The feature visualizations of the 2-class catalog and 3-class catalog after FFT-CNN are shown in Figs. 12 and 13, respectively.

In order to verify the stability of the proposed method, the proposed model is tested ten times to derive the final classification result. The classification accuracies on the 2-class catalog consisting of earthquake and tsunami (1), earthquake and volcano (2), and tsunami and volcano (3) are shown in Fig. 14. The classification accuracies of the two architectures on the 3-class catalog consisting of signals from earthquake, tsunami, and volcano (4) are also presented in Fig. 14. As shown in Fig. 14, the classification accuracy of VMD-FFT-CNN is higher than the FFT-CNN model by nearly 5%, which shows that the VMD denoising process is effective. This implies that VMD-FFT-CNN has a good classification performance.

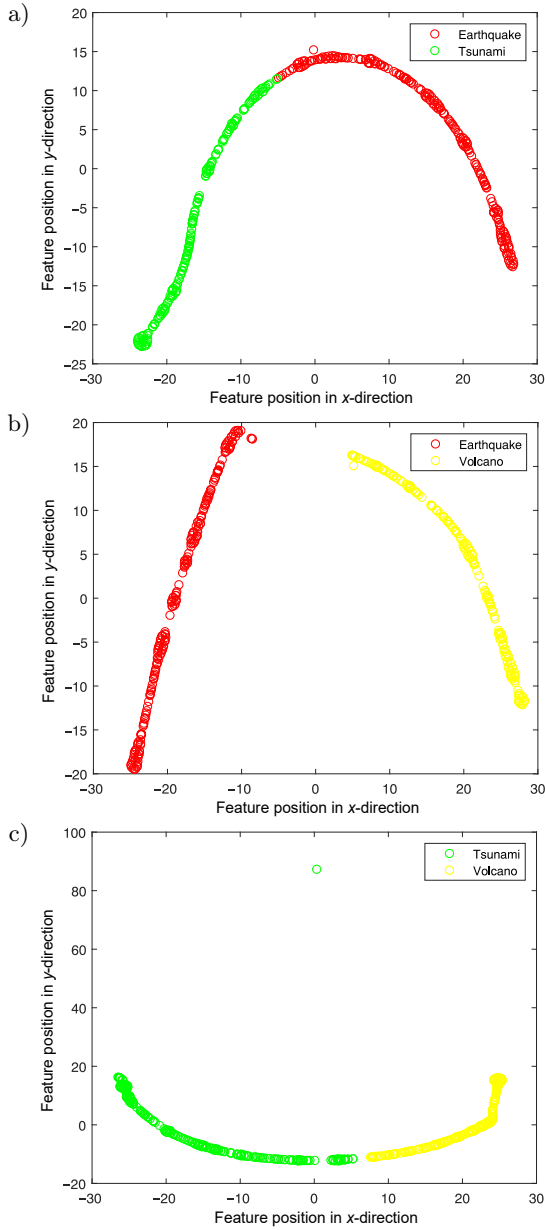


Fig. 8. Feature visualization of the 2-class catalog after VMD-FFT-CNN: a) earthquake and tsunami; b) earthquake and volcano; c) tsunami and volcano.

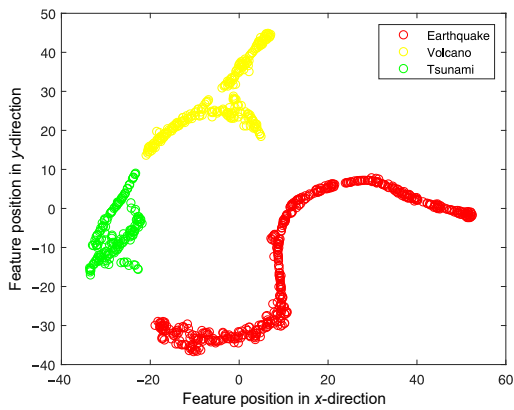


Fig. 9. Feature visualization of the 3-class catalog after VMD-FFT-CNN.

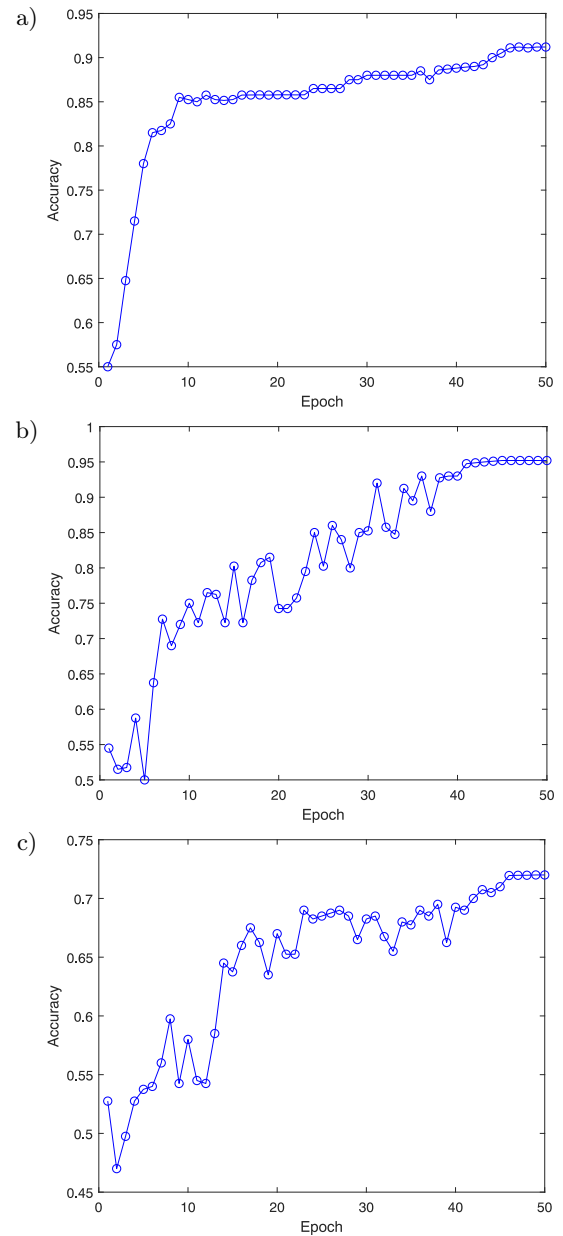


Fig. 10. Classification accuracy of the 2-class catalog after FFT-CNN: a) earthquake and tsunami; b) earthquake and volcano; c) tsunami and volcano.

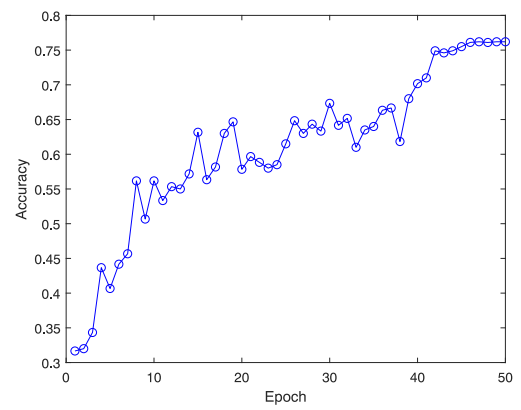


Fig. 11. Classification accuracy of the 3-class catalog after FFT-CNN.

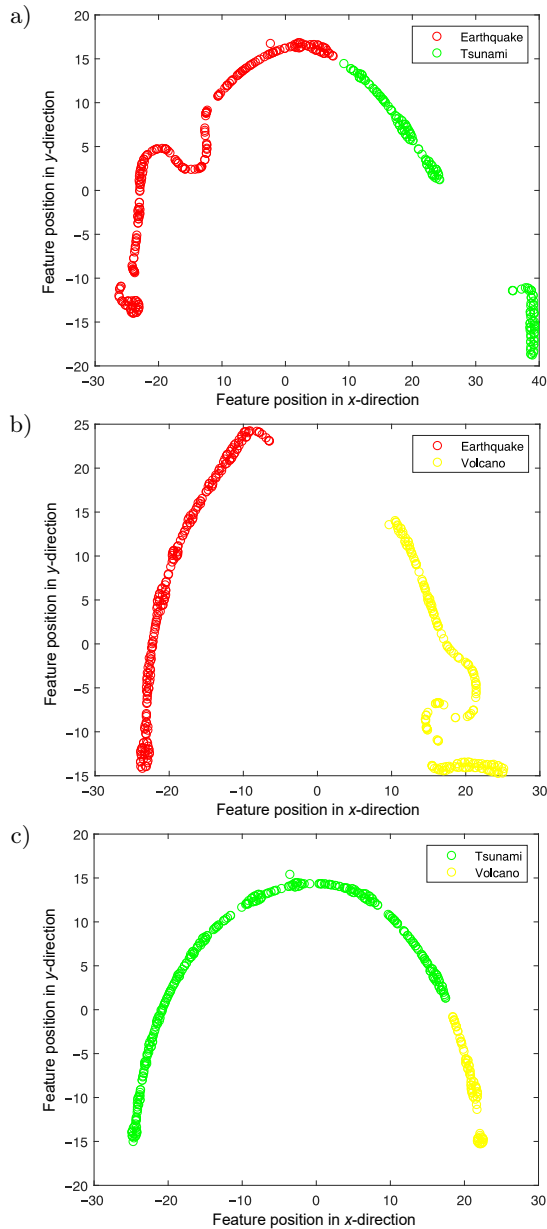


Fig. 12. Feature visualization of the 2-class catalog after FFT-CNN: a) earthquake and tsunami; b) earthquake and volcano; c) tsunami and volcano.

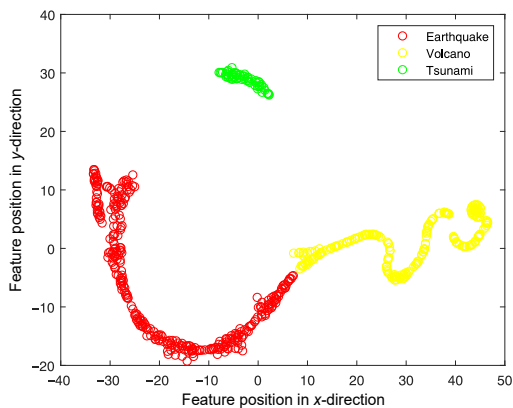


Fig. 13. Feature visualization of the 3-class catalog after FFT-CNN.

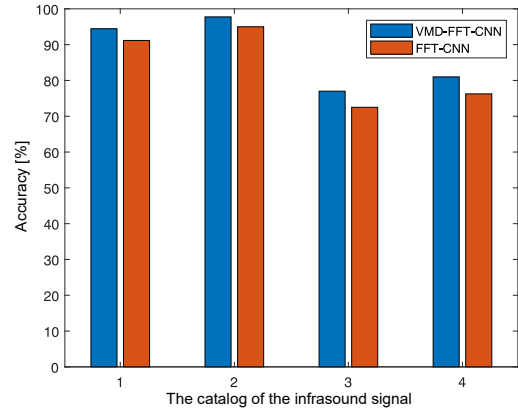


Fig. 14. Accuracy of two methods.

### 4. Discussion

VMD-FFT-CNN outperforms the FFT-CNN approach in the denoising process. VMD-FFT-CNN has high performance for infrasound signal identification and can achieve 97.75% and 81% of the 2-class catalog and 3-class catalog classification accuracies, respectively. The proposed approach shows excellent performance in classification accuracy compared with other methods and shows a good robustness under noisy environments. For example, the classification accuracy of VMD-FFT-CNN on the 2-class catalog consisting of earthquakes and volcanic increases by 23.25% compared with CNN (ALBERT, LINVILLE, 2020). This result demonstrates that the model presented in this paper has good accuracy for infrasound signal classification. As shown in Fig. 3, the source locations are widespread but their number is small. Due to the limitation of the data, the proposed approach may not be generalized for global hazard monitoring.

### 5. Conclusion and future work

This paper proposed a valid classification and identification method for the infrasound signal of disasters. The infrasound signal was processed by VMD to eliminate the noise. FFT was used to convert the reconstructed signal into a frequency domain image. A CNN model was constructed for automatically extracting the features and classifying the infrasound signals. The experiment results show that the proposed approach improves the accuracy of geophysical monitoring.

Due to the limitations of the existing conditions, tests can only use small samples and a few infrasound types, which will affect the reliability of the test results. In order to obtain more accurate results, more infrasound data and infrasonic event types should be analyzed. For future work, real-time infrasound signal classification will be carried out and further study on infrasound types will be performed. Deep learning

should be developed for global infrasound signal classification.

### Acknowledgments

This work was supported by the National Natural Science Foundation of China (grant no. 41572347), Graduate Innovation Fund Project of China University of Geosciences, Beijing (YB2021YC020). Many thanks to the Comprehensive Nuclear-Test-Ban Treaty Beijing National Data Center for providing the data.

### References

- ALBERT S., LINVILLE L. (2020), Benchmarking current and emerging approaches to infrasound signal classification, *Seismological Research Letters*, **91**(2A): 921–929, doi: [10.1785/0220190116](https://doi.org/10.1785/0220190116).
- ASMING V.E., FEDOROV A.V., FEDOROV I.S., ASMING S.V. (2022), Algorithms for the detection, location, and discrimination of seismic and infrasound events, *Izvestiya, Atmospheric and Oceanic Physics*, **58**(11): 1398–1417, doi: [10.1134/S0001433822110019](https://doi.org/10.1134/S0001433822110019).
- COFFERB B.E., PARKER M.D. (2022), Infrasound signals in simulated nontornadic and pre-tornadic supercells, *The Journal of the Acoustical Society of America*, **151**(2): 939–954, doi: [10.1121/10.0009400](https://doi.org/10.1121/10.0009400).
- DE ANGELIS S., DIAZ-MORENO A., ZUCCARELLO L. (2019), Recent developments and applications of acoustic infrasound to monitor volcanic emissions, *Remote Sensing*, **11**(11): 1302, doi: [10.3390/rs11111302](https://doi.org/10.3390/rs11111302).
- DRAGOMIRETSKIY K., ZOSSO D. (2014), Variational mode decomposition, *IEEE Transactions on Signal Processing*, **62**(3): 531–544, doi: [10.1109/TSP.2013.2288675](https://doi.org/10.1109/TSP.2013.2288675).
- ECKEL F., LANGER H., SCIOTTO M. (2023), Monitoring sources of volcanic activity at Mount Etna using pattern recognition techniques on infrasound signals, *Geophysical Journal International*, **232**(1): 1–16, doi: [10.1093/gji/ggac278](https://doi.org/10.1093/gji/ggac278).
- GARCIA R.F. *et al.* (2021), Search for infrasound signals in InSight data using coupled pressure/ground deformation methods, *Bulletin of the Seismological Society of America*, **111**(6): 3055–3064, doi: [10.1785/0120210079](https://doi.org/10.1785/0120210079).
- GARCIA R.F. *et al.* (2022), Infrasound from large earthquakes recorded on a network of balloons in the stratosphere, *Geophysical Research Letters*, **49**(15): e2022GL098844, doi: [10.1029/2022GL098844](https://doi.org/10.1029/2022GL098844).
- GI N., BROWN P. (2017), Refinement of bolide characteristics from infrasound measurements, *Planetary and Space Science*, **143**: 169–181, doi: [10.1016/j.pss.2017.04.021](https://doi.org/10.1016/j.pss.2017.04.021).
- HAM F.M., REKAB K., ACHARYYA R., LEE Y.-C. (2008), Infrasound signal classification using parallel RBF Neural Networks, *International Journal of Signal and Imaging Systems Engineering*, **1**(3–4): 155–167, doi: [10.1504/IJSISE.2008.026787](https://doi.org/10.1504/IJSISE.2008.026787).
- HUPE P., CERANNA L., LE PICHON A., MATOZA R.S., MIALLE P. (2022), International Monitoring System infrasound data products for atmospheric studies and civilian applications, *Earth System Science Data*, **14**(9): 4201–4230, doi: [10.5194/essd-14-4201-2022](https://doi.org/10.5194/essd-14-4201-2022).
- IEZZI A.M., SCHWAIGER H.F., FEE D., HANEY M.M. (2019), Application of an updated atmospheric model to explore volcano infrasound propagation and detection in Alaska, *Journal of Volcanology and Geothermal Research*, **371**: 192–205, doi: [10.1016/j.jvolgeores.2018.03.009](https://doi.org/10.1016/j.jvolgeores.2018.03.009).
- LAWRENCE S., GILES C.L., TSOI A.C., BACK A.D. (1997), Face recognition: A convolutional neural-network approach, *IEEE Transactions on Neural Networks*, **8**(1): 98–113, doi: [10.1109/72.554195](https://doi.org/10.1109/72.554195).
- LENG X.-P., LIU D.-L., WEI F.-Q., HONG Y., DAI D.-F. (2017), Debris flows monitoring and localization using infrasonic signals, *Journal of Mountain Science*, **14**(7): 1279–1291, doi: [10.1007/s11629-016-3836-3](https://doi.org/10.1007/s11629-016-3836-3).
- LI M., LIU X.Y., LIU X. (2016), Infrasound signal classification based on spectral entropy and support vector machine, *Applied Acoustics*, **113**: 116–120, doi: [10.1016/j.apacoust.2016.06.019](https://doi.org/10.1016/j.apacoust.2016.06.019).
- LIU D., TANG D., ZHANG S., LENG X., HU K., HE L. (2021), Method for feature analysis and intelligent recognition of infrasound signals of soil landslides, *Bulletin of Engineering Geology and the Environment*, **80**(2): 917–932, doi: [10.1007/s10064-020-01982-w](https://doi.org/10.1007/s10064-020-01982-w).
- LIU X.Y., LI M., TANG W., WANG S.C., WU X. (2014), A new classification method of infrasound events using Hilbert-Huang transform and support vector machine, *Mathematical Problems in Engineering*, **2014**(3): 1–6, doi: [10.1155/2014/456818](https://doi.org/10.1155/2014/456818).
- MAYER S., VAN HERWIJNEN A., ULIVIERI G., SCHWEIZER J. (2020), Evaluating the performance of an operational infrasound avalanche detection system at three locations in the Swiss Alps during two winter seasons, *Cold Regions Science and Technology*, **173**: 102962, doi: [10.1016/j.coldregions.2019.102962](https://doi.org/10.1016/j.coldregions.2019.102962).
- PERTTU A., TAISNE B., DE ANGELIS S., ASSINK J.D., TAILPIED D., WILLIAMS R.A. (2020), Estimates of plume height from infrasound for regional volcano monitoring, *Journal of Volcanology and Geothermal Research*, **402**: 106997, doi: [10.1016/j.jvolgeores.2020.106997](https://doi.org/10.1016/j.jvolgeores.2020.106997).
- THÜRING T., SCHOCH M., VAN HERWIJNENA A., SCHWEIZER J. (2015), Robust snow avalanche detection using supervised machine learning with infrasonic sensor arrays, *Cold Regions Science and Technology*, **111**: 60–66, doi: [10.1016/j.coldregions.2014.12.014](https://doi.org/10.1016/j.coldregions.2014.12.014).
- VAN DER MAATEN L., HINTON G. (2008), Visualizing data using t-SNE, *Journal of Machine Learning Research*, **9**(11): 2579–2605.
- WATSON L.M. *et al.* (2022), Volcano infrasound: progress and future directions, *Bulletin of Volcanology*, **84**(5): 44, doi: [10.1007/s00445-022-01544-w](https://doi.org/10.1007/s00445-022-01544-w).

23. WITSIL A., FEE D., DICKEY J., PEÑA R., WAXLER R., BLOM P. (2022), Detecting large explosions with machine learning models trained on synthetic infrasound data, *Geophysical Research Letters*, **49**(11): e2022GL097785, doi: [10.1029/2022GL097785](https://doi.org/10.1029/2022GL097785).
24. WITSIL A.J., JOHNSON J.B. (2020), Analyzing continuous infrasound from Stromboli volcano, Italy using unsupervised machine learning, *Computers & Geosciences*, **140**: 104494, doi: [10.1016/j.cageo.2020.104494](https://doi.org/10.1016/j.cageo.2020.104494).
25. YANG X., SU W., JIANG C., BIAN Y. (2022), Research progress on infrasound generation mechanism, monitoring technology and application, *Progress in Geophysics*, **37**(1): 78–93, doi: [10.6038/pg2022FF0081](https://doi.org/10.6038/pg2022FF0081).
26. ZHANG M., GAO L., ZHANG X., ZHANG S. (2022), An infrasound source localisation algorithm for improving location accuracy of gas pipeline leakage detection system, *International Journal of Embedded Systems*, **15**(1): 9–18, doi: [10.1504/IJES.2022.122042](https://doi.org/10.1504/IJES.2022.122042).
27. ZHANG S. *et al.* (2020), Model test: Infrasonic features of porous soil masses as applied to landslide monitoring. *Engineering Geology*, **265**: 105454, doi: [10.1016/j.enggeo.2019.105454](https://doi.org/10.1016/j.enggeo.2019.105454).
28. ZHU X., XU Q., LIU H.X. (2017), Using Hilbert-Huang transform (HHT) to extract infrasound generated by the 2013 Lushan earthquake in China, *Pure and Applied Geophysics*, **174**(3): 865–874, doi: [10.1007/s00024-016-1438-1](https://doi.org/10.1007/s00024-016-1438-1).